

Detection and imaging sensitivity of the marine CSEM method

Rune Mittet¹ and Jan Petter Morten¹

ABSTRACT

We have developed a formalism to systematically study the sensitivity of the marine controlled source electromagnetic method for hydrocarbon exploration, taking into account measurement errors. We utilize error propagation to estimate the data uncertainty, and find that contributions that scale by the transmitter dipole moment give qualitatively different behavior than noise contributions that are independent of the dipole moment. The uncertainty is used in quantitative criteria to determine if a hydrocarbon reservoir can be detected and whether it can be successfully imaged. Our formalism can be used to make detailed feasibility studies incorporating equipment accuracy limitations, and to identify which experimental component that must be improved to ensure overall improvement in sensitivity. The criteria can be applied to identify the limiting factors for detection and imaging of targets with increasing burial depth. We have defined experimental accuracy conditions for next generation CSEM equipment to successfully image a large hydrocarbon reservoir at 5 km burial depth.

INTRODUCTION

The marine controlled source electromagnetic (CSEM) method was introduced as a tool for hydrocarbon reservoir detection more than a decade ago (Eidesmo et al., 2002; Ellingsrud et al., 2002). The large-scale resistivity information that can be derived from the CSEM data can be correlated to fluid type. Marine CSEM is therefore a complementary method to the marine seismic method in hydrocarbon exploration, mainly because the electromagnetic data are more sensitive to hydrocarbons than the seismic data. The development of the method was recently reviewed in Constable (2010).

Marine CSEM is today routinely acquired in very diverse environments including water depths ranging from 40 m to ultradeep.

The survey objectives may also vary from mapping of salt structures and regional studies to prospect ranking and appraisal. The limiting factors for the successful application of the CSEM technology include ambiguity of interpretation, low resolution, and measurement uncertainty. In this paper, we study the experimental conditions that may affect the ability to detect and image a hydrocarbon reservoir. This problem has previously been addressed in the context of CSEM time-lapse measurements (Orange et al., 2009; Zach et al., 2009), and for interpretation of 1D inversion results (Myer et al., 2010).

The marine CSEM method is inherently a low-frequency method. The problem is not to generate electromagnetic fields with high frequencies, but the strong attenuation of the electromagnetic fields in a conductive formation. If we want to detect an object in the subsurface, we need not only for the electromagnetic field to reach that object; the field must come back to the receiver, and it needs to do so with an amplitude that is above the measurement uncertainty. Signal attenuation increases with increasing frequency. To image a deep target, the solution is not to use very low frequencies only because in that case we may lose resolution of objects that are small compared to the transmitted wavelength, but are still of sufficient size to be of interest in hydrocarbon exploration. The frequency band used in a marine CSEM survey often reflects a trade-off between the desire to have high frequencies for the resolution and low frequencies for the penetration.

One of the points we make in this paper is that there can be a fairly large difference between the maximum depth of detection and the maximum depth of imaging for the marine CSEM method. By imaging we mean that the main features of a resistive object like a hydrocarbon saturated reservoir can be recovered by inversion. Loosely speaking, we can say that the maximum depth of detection is defined by the case where the scattered field from an object is above the recording equipment noise level. The conditions for successful imaging and parameter recovery by inversion are more strict and require that the scattered field is well above the recording equipment noise level. The maximum depth of detection can be up to 1000 m larger than the maximum depth of imaging. Typical maximum depth of imaging in a conductive formation is today 2500 m,

Manuscript received by the Editor 13 January 2012; revised manuscript received 15 May 2012; published online 12 October 2012.

¹EMGS ASA, Trondheim, Norway. E-mail: rm@emgs.com; jpmorten@emgs.com.

© 2012 Society of Exploration Geophysicists. All rights reserved.

but our practical experience from inversion of real data is that it can be as large as 3500 m or more if the resistivity increases sufficiently with depth. These numbers are based on a transmitter frequency of 0.25 Hz, which gives a fair trade off between penetration depth and resolution. A reduced transmitter frequency will increase the maximum depth of imaging at the potential cost of reduced resolution. The number of potential targets for the marine CSEM method will increase by a factor of two if we can shift this scenario (2500 m) to a maximum depth of imaging of 4000 m.

Let us assume that we have determined a minimum frequency necessary for sufficient resolution, then the obvious ways to achieve an increased depth of imaging are to increase receiver sensitivity and to increase transmitter output current. We will demonstrate below how the two strategies have different impacts on measurement uncertainty. We have chosen to analyze the sensitivity dependence on increasing target burial depth by applying error propagation analysis and derive a systematic approach to determine sensitivity limiting measurement errors. We view this analysis as part of the toolbox for guiding the development of the next generation marine CSEM equipment. In the “Results” section, we apply the formalism to consider the limitations of current state-of-the-art instrumentation, and show how next generation equipment must be improved to enhance the detection and imaging capability.

THEORY

A mathematical model that can be used to study the measurement uncertainty of CSEM data must take into account parameters that describe the environment like, e.g., overburden conductivity, and a range of parameters that describe the experimental configuration. In this section, we will describe such a model, and derive the predicted data uncertainty.

Model

We will analyze the following model for the measured electrical field E_i component $i = x, y, z$ recorded at position \mathbf{r}_r due to an electric dipole transmitter at \mathbf{r}_s :

$$E_i(\mathbf{r}_r, \omega | \mathbf{r}_s) = F \left[\sum_{j,k} R_{ij} G_{jk}^{EJ}(\mathbf{r}_s, \omega | \mathbf{r}_s) L J_k(\mathbf{r}_s, \omega) + N_A(\omega) \right] + N_R(\omega). \quad (1)$$

Here, R_{ij} is a rotation matrix in three dimensions that describes the orientation of the receiver sensors, G_{jk}^{EJ} is an ideal/noiseless Green’s function from a given conductivity distribution, L is the length of the transmitter antenna, and J_k is the transmitter current for component k . The angular frequency is $\omega = 2\pi f$, where f is frequency. We have included two noise terms that describe ambient noise $N_A(\omega)$ and receiver self-noise $N_R(\omega)$, which will be described below. Although we study the electrical field specifically, the same model can be applied to study magnetic field measurements.

The function F in equation 1 describes the relation between the actual electric field and the measured value. This relationship can be parameterized as

$$F[E_i(\omega), \omega] = a(|E_i(\omega)|) e^{ib(\arg\{E_i(\omega)\}, \omega)}, \quad (2a)$$

$$a(|E|) = \alpha|E| + \eta, \quad (2b)$$

$$b(\arg\{E_i\}, \omega) = \beta \arg\{E_i(\omega)\} + \omega\tau. \quad (2c)$$

The real parameters α , β , η , and τ describe the performance of the receiver experimental components in terms of scaling and shift behaviors. The measured values may deviate from the actual field if these parameters differ from the nominal values. The nominal value of α and β is one, and the nominal value of η and τ is zero. The parameters α and β are, in principle, frequency-dependent. However, for the frequency band normally encountered in marine CSEM, they can be considered constant with frequency. This will not necessarily be the case for MT data due to the much larger frequency band. A deviation from the nominal value for τ corresponds physically, e.g., to the effect of imperfectly synchronized clocks on the transmitter and the receiver, which will induce a small but measurable time shift. The parameter η describes a constant amplitude shift, caused, e.g., by a voltage offset in the equipment. The amplitude and phase scaling parameters α and β may deviate from their nominal value if the amplitude calibration table of the equipment is inaccurate due to, e.g., aging effects in the sensors. Quality control of data from short source-receiver offset can typically determine if β and τ deviate from their nominal values. The definition of the phase-scaling factor β requires that the complex argument function (\arg) represents the unwrapped phase, i.e., it determines the phase as a monotonous function of the source-receiver offset.

Experimentally, it is challenging to mitigate fluctuations in the parameters of equation 2. Receivers are deployed in a harsh environment and calibration is necessary between each drop. The deviation from nominal values may depend on the accuracy of the on-board calibration equipment. This calibration equipment must be very accurate to keep uncertainty at a minimum.

The transmitter is modeled as a straight, extended dipole with length L in equation 1. This length is typically close to 300 m and can be measured with high accuracy. If the equipment is not rigid, fluctuations from this value can occur when the transmitter is not completely straight. This typically leads to a reduction of L . In equation 1, we use an approximate representation of the transmitter which is valid when we consider data from offsets above 2 km, and for the frequencies used in the examples to follow. To study the near-field data uncertainty, the correct formal transmitter representation is obtained by integrating the Green’s function multiplied with an infinitesimal electric dipole over the length of the transmitter.

The transmitter current amplitude is described by the magnitude of the vector \mathbf{J} in equation 1. Typical values for current equipment are 1–1.5 kA, but it is feasible to increase the transmitter current to 10 kA. The current \mathbf{J} is in principle a vector of complex numbers in the frequency domain, but will be treated as a real vector here. The reason is that we can choose the origin of the temporal axis such that the current phase is zero, and we included the phase shift τ in equation 2c to account for clock synchronization mismatch between the receiver and the transmitter. The vector nature of the source current will be described in terms of the heading ϕ_s and pitch θ_s angles of the towed transmitter,

$$\mathbf{J} = J(\cos \theta_s \cos \phi_s, \cos \theta_s \sin \phi_s, \sin \theta_s). \quad (3)$$

In the inline CSEM configuration, heading and pitch angles have a nominal value of zero for a horizontal transmitter. This is the configuration we will analyze here.

We included the term N_A in equation 1 to account for sources of ambient noise that are independent of the electromagnetic field generated by the transmitter. Generally, this term is given by the superposition of different contributions:

$$N_A(\omega) = N_{MT}(\omega) + N_{SW}(\omega) + N_V(\omega). \quad (4)$$

In this equation, the term N_{MT} gives the amplitude of the magnetotelluric (MT) signal. The MT signal is typically a challenge in shallow water and at high latitudes. MT signals are spatially correlated, and can be subtracted by multistation analysis to reduce the contribution of N_{MT} (de la Kethulle de Ryhove and Maaø, 2008). The term N_{SW} gives the amplitude of the ocean swell noise. The swell noise contribution is typically a problem in shallow water only. Depending on weather conditions, this noise is typically small for frequencies above 0.1 Hz. The amplitude spectrum of N_{SW} can be determined by real-time measurements at the survey location before transmitter towing starts. In that way, the survey frequencies can be chosen to avoid the frequency bands that have the largest contributions from the swell noise. Figure 1 shows a spectrogram from a receiver deployed at 40-m water depth. The swell noise can be seen as a band of increased background noise at frequencies below 0.1 Hz. The CSEM survey frequencies were chosen above this level. In the figure, two time intervals of transmitter towing close to the receiver can be identified from the large amplitudes.

The term N_V in equation 4 represents the electromagnetic noise due to vibrations in the receiver unit and the electrode arms. This contribution is typically a problem in the presence of strong tidal water currents. The vibration-induced noise can be reduced by designing receivers and electrode arms with a shape that reduces the hydrodynamic interactions.

The magnitude of the contributions to N_A in equation 4 depends on uncontrollable parameters like weather conditions, as well as details about the survey area like water depth and latitude. Therefore, the actual level for N_A must typically be determined from the measured data.

The term N_R in equation 1 describes the contribution from the receiver self-noise. This noise is related to sensor thermal noise and amplifier voltage noise. The amplifier current noise is small in comparison to these contributions. The receiver self-noise spectrum has a $1/f$ dependence up to 0.1 Hz, and a constant level above this frequency. Noise estimates can be given in different ways. Here, we assume an electrode separation of 8 m and a time-to-frequency transform window of length 200 s. For sensors and amplifiers in use today, the receiver self-noise fluctuates at amplitudes up to 10^{-10} V/m above 0.1 Hz. We expect that the next generation of receivers will have an order of magnitude smaller noise amplitude down to frequencies of order mHz. Here, and for the rest of this paper, we have chosen to quantify the noise in units of V/m. It is not uncommon to normalize the noise by the transmitter dipole moment (Constable, 2010). Both approaches are valid as long as they are applied consistently. Our choice is guided by the fact that several of the noise sources we discuss are independent of the transmitter dipole moment. It is also a natural choice because our data are simulated with realistic transmitter currents and transmitter lengths.

In the following analysis, we have chosen to assimilate the effect of N_A into N_R in equation 1. When receiver calibration is good and the parameters in equation 2 are close to their nominal value, the effect of N_A is equivalent to that of N_R in our formalism. In that

case, we need only to set the level of fluctuations in N_R to reflect both contributions.

Error propagation

We will now derive the data uncertainty δE_i following from uncertain experimental parameters in the model equation 1. At the same time, we will discuss relative magnitudes of the parameters and describe which can be disregarded in the analysis. Some of the contributions will be calculated numerically using plane layer models. The proposed methodology can be generalized to models with complicated 3D geometries, but we believe that plane layer modeling captures the most important contributions to the uncertainty for marine CSEM.

Because we have chosen a plane layer assumption for the remaining analysis, we note that the electromagnetic fields in this case do not depend separately on the source and receiver coordinates. In the laterally invariant model, the measurements depend on the lateral and vertical source-receiver offset, which we define as $x = \sqrt{r_x^2 + r_y^2}$ and $z = r_z$, where $\mathbf{r} = \mathbf{r}_r - \mathbf{r}_s$. The stationary receiver is in practice easier to position accurately compared to the transmitter. Receivers can be positioned with an accuracy of ± 2 m or better, if required. This accuracy decreases with increasing water depth. The transmitter moves during acquisition, and as such is harder to position. To simplify the analysis, we assume in the following that all navigation uncertainty is related to the transmitter, which has the dominant contribution. The accuracy with existing technology is $\Delta x = \pm 15$ m in the lateral direction, and $\Delta z = \pm 5$ m in the vertical direction.

The rotation matrix R_{ij} depends on the three angles that describe the orientation of the receiver. These angles are experimental parameters that introduce measurement uncertainty. The receiver pitch and roll angles are nonzero when the bathymetry is not flat. These angles can be measured accurately by tilt sensors mounted on the receiver frame, and we neglect errors due to inaccurate receiver pitch and roll. The receiver yaw angle ϕ_r , or orientation with respect to north, is more difficult to determine experimentally. Typically, it is determined by data-driven methods (Morten et al., 2010) to an accuracy $\Delta\phi_r = \pm 2^\circ$. In the following, we will restrict the analysis to inline electric field data. The inline data come from the field component parallel to the towline when the transmitter is towed along a line that passes directly over the receiver position on the seafloor.

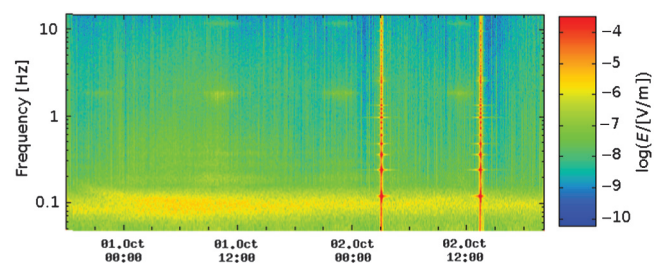


Figure 1. Measured spectrogram for component E_z from a receiver deployed in shallow water. The swell noise constitutes a band of increased noise below 0.1 Hz. The tick marks on the horizontal axis denote days, and the color scale is $\log(E/[V/m])$, where E is the magnitude of a component of the electric field. The contribution from swell noise is qualitatively similar in spectrograms for other field components.

These measurements will have the strongest response from hydrocarbon reservoirs in CSEM data. We choose a coordinate system where the towline coincides with the x -axis, and consider E_x data. The electric field component perpendicular to the towline E_y will then have a negligible amplitude due to the symmetries of the problem. As explained by Morten et al. (2009), the contribution to measurement uncertainty in E_x due to $\Delta\phi_r$ will scale with E_y , and therefore be negligible in this context. Note that uncertainty in ϕ_r is important in 3D geometries, and when data from receivers off the towline are considered.

The accuracy and stability of the transmitted frequency is very good, so we assume that there are no issues related to uncertainty in ω . The ω argument is implicit for the rest of the paper. Moreover, we will assume that the uncertainty contributions from β and η in equation 2 are negligible. These parameters are related to magnitude shift and phase scaling, for which errors in receiver calibration are typically very small. Therefore, we set these parameters to their nominal values $\beta = 1$ and $\eta = 0$. We have now defined all the experimental quantities which will give significant contributions to the data uncertainty in the model equation 1. Let us collect these quantities in a parameter vector:

$$\mathbf{p} = [\mathbf{r}, \alpha, \tau, J, L, \theta_s, \phi_s, N_R]^T.$$

According to linear error propagation, valid when uncertainty in each parameter is small, the total uncertainty in the inline electric field can be computed as

$$\delta E_x(\mathbf{p}) = \sqrt{\sum_{m,n} (\partial_{p_m} E_x) C_{mn} (\partial_{p_n} E_x)^*}. \quad (5)$$

The partial derivatives should be evaluated for the nominal value of all the parameters in \mathbf{p} . We introduced the covariance matrix C_{mn} for quantities at components m and n in the parameter vector \mathbf{p} , which takes into account situations where two errors are correlated. A typical example of correlated quantities in CSEM data is the source position and pitch, which are determined from the sensor data on the head and the tail of the transmitter. For the receiver, we can in some cases expect that our model parameters α and β have correlated contributions to the error because they are affected by inaccurate receiver calibration. In the following analysis, we will assume that the additional uncertainty contributions due to correlations are smaller than the contribution from uncorrelated errors, i.e., we neglect contributions when $m \neq n$ in equation 5. We can then simplify the expression for the inline data uncertainty,

$$\delta E_x(\mathbf{p}) = \sqrt{\sum_n [\delta E_x(p_n)]^2}, \quad (6)$$

where we defined

$$\delta E_x(p_n) = |\partial_{p_n} E_x(\mathbf{p})| |\Delta p_n|. \quad (7)$$

The quantity $\delta E_x(p_n)$ determines the individual contribution to the uncertainty from parameter p_n if all other quantities are measured without error. Let us now consider how to determine these contributions.

For convenience, we define the quantity $D = \alpha L J e^{i\omega\tau}$ which is equal to the transmitter dipole moment when $\alpha = 1$ and $\tau = 0$. The data uncertainty due to uncertain spatial positioning will then depend on the derivatives,

$$\partial_x E_x(\mathbf{p}) = \partial_x G_{xx}^{EJ}(\mathbf{r}) D, \quad (8a)$$

$$\partial_z E_x(\mathbf{p}) = \partial_z G_{xx}^{EJ}(\mathbf{r}) D. \quad (8b)$$

These factors will be calculated numerically. The contribution from equation 8a can be relatively large. This is because it captures the effect of the uncertainty in transmitter-receiver offset in the inline direction, where the amplitude decays exponentially with increasing offset. The partial derivative with respect to y is assumed smaller and neglected. The reason is that a small deviation in this direction does not change the source-receiver distance or relative angle significantly if the source-receiver distance is above 1–2 km. However, the variation with depth from equation 8b cannot be neglected because the transmitter is close to the seabed and the conductivity change here is significant.

The term related to clock synchronization gives

$$\partial_\tau E_x(\mathbf{p}) |_{\tau=0} = G_{xx}^{EJ}(\mathbf{r}_r | \mathbf{r}_s) D i\omega. \quad (9)$$

The partial derivatives in equation 7 related to receiver calibration, transmitter current magnitude, and transmitter length behave in a similar manner:

$$\partial_\alpha E_x(\mathbf{p}) = G_{xx}^{EJ}(\mathbf{r}) D \frac{1}{\alpha}, \quad (10a)$$

$$\partial_J E_x(\mathbf{p}) = G_{xx}^{EJ}(\mathbf{r}) D \frac{1}{J}, \quad (10b)$$

$$\partial_L E_x(\mathbf{p}) = G_{xx}^{EJ}(\mathbf{r}) D \frac{1}{L}. \quad (10c)$$

Let us now consider the uncertainty related to the orientation of the transmitter. The cosine factors in equation 3 give sines when differentiated with respect to ϕ_s or θ_s . Because the nominal value for these angles is zero in the inline configuration, such factors will not contribute to the linear order which we consider here. The factor G_{xy}^{EJ} is zero in the inline case. The surviving term that potentially can have an impact is

$$\partial_{\theta_s} E_x(\mathbf{p}) |_{\theta_s=0} = G_{xz}^{EJ}(\mathbf{r}) D. \quad (11)$$

This term will introduce dependence on uncertainty in the transmitter pitch angle, denoted $\Delta\theta_s$.

The differentiation with respect to the noise term is trivial,

$$\partial_{N_R} E_x(\mathbf{p}) = 1. \quad (12)$$

The nominal value for the noise is zero, but noise fluctuations will contribute with a magnitude described by ΔN_R .

We have now considered all the differentiations involved in the expression for the total uncertainty, equation 5. The partial contributions described by the terms defined in equation 6 become

$$\delta E_x(x) = |\partial_x G_{xx}^{EJ}(\mathbf{r}) D \Delta x|, \quad (13a)$$

$$\delta E_x(z) = |\partial_z G_{xx}^{EJ}(\mathbf{r}) D \Delta z|, \quad (13b)$$

$$\delta E_x(c) = \left| G_{xx}^{EJ}(\mathbf{r})D \right| \times \sqrt{\left(\frac{\Delta\alpha}{\alpha}\right)^2 + \left(\frac{\Delta J}{J}\right)^2 + \left(\frac{\Delta L}{L}\right)^2 + (\omega\Delta\tau)^2}, \quad (13c)$$

$$\delta E_x(\theta) = |G_{xz}^{EJ}(\mathbf{r})D\Delta\theta_s|, \quad (13d)$$

$$\delta E_x(N) = |\Delta N_R|. \quad (13e)$$

The terms proportional to the field amplitude are grouped together in equation 13c and we define the parameter c to denote their combined contribution. Here, we introduce the uncertainties in receiver calibration $\Delta\alpha$, source current ΔJ , and transmitter length ΔL . We will disregard the phase shift contribution $\omega\Delta\tau$ due to timing uncertainty $\Delta\tau$ in the following because it is small. This is because the transmitter clock and the receiver clock are time-stamped on the same GPS signal. The receiver clock is drift-corrected when it is retrieved from the seabed. The value of $\Delta\tau$ is less than 10 μs , so for normal CSEM frequencies below 10 Hz, the contribution from the three other terms will be more than one order of magnitude larger.

The resulting total uncertainty can now be written

$$\delta E_x(\mathbf{p}) = \sqrt{[\delta E_x(M)]^2 + [\delta E_x(N)]^2}, \quad (14)$$

where all the terms proportional to the electromagnetic field or its partial derivative with respect to one of the parameters are contained in $\delta E_x(M)$,

$$[\delta E_x(M)]^2 = [\delta E_x(x)]^2 + [\delta E_x(z)]^2 + [\delta E_x(c)]^2 + [\delta E_x(\theta)]^2. \quad (15)$$

The expression in equation 14 summarizes our prediction of data uncertainty following from the model in equation 1.

Detection and imaging criteria

We would like to quantify whether or not a given experimental system is sensitive to a resistive target. This will depend on the relative magnitude of data target response to the magnitude of the uncertainty that we have derived above. The most widely used and reliable way to interpret CSEM data today is inversion. However, we propose a procedure to determine limiting criteria for detection and imaging that does not require us to run an inversion for each case. Inversion algorithms are typically optimizations that attempt to minimize the difference between the observed data and the predicted data. Due to nonlinearity, this is done iteratively and at iteration n the data difference is

$$\Delta E_x^n(\mathbf{p}) = E_x^{\text{Obs}}(\mathbf{p}) - E_x^n. \quad (16)$$

Here, we defined E_x^n as the synthetic data at iteration n . To improve the model in the next iteration, this data difference must be larger than the uncertainty in the data for some offset interval. We will assume that any modeling errors inherent in E_x^n will be negligible compared to the experimental uncertainty.

We introduce the ratio of the data difference to the total uncertainty,

$$\Psi^n(\mathbf{p}) = \left| \frac{\Delta E_x^n(\mathbf{p})}{\delta E_x(\mathbf{p})} \right|, \quad (17)$$

and require that this ratio must be larger than unity for some offsets to proceed to iteration $n + 1$. If the data difference is less than the uncertainty in the data for all offsets, i.e., $\Psi^n(\mathbf{p}) \lesssim 1$, there is no more geologic information accessible from the data. The inversion could then only proceed by adjusting the model according to eventual regularization terms.

We focus on two values of n in particular. For the initial model, $n = 0$, we assume in the examples to follow that no information on the resistive target is available. The ratio Ψ^0 can serve as a sensitivity measure if the initial model describes the actual background well. Proper background models can be achieved by incorporating other geophysical data like, e.g., seismic and well log data, and by inversion of CSEM data that were not directly sensitive to the target. The contribution from a resistive target will then be present in the observed data, but not in the predicted data from the initial model. For this case, we will refer to the data difference in equation 17 as the scattered field. If the scattered field is larger than the experimental uncertainty, then it is reasonable to assume that we can detect the resistive target.

The depth of investigation will be limited by the detection criterion due to the decay of the electromagnetic signals propagating through the overburden. It is important to individually inspect the contribution to the total uncertainty $\delta E_x(\mathbf{p})$ from each contributing term to determine how the experimental equipment can be improved to increase the depth of investigation. The largest term may be viewed as an identifier to the weakest link in the experimental configuration because the total uncertainty cannot be reduced below the individual contribution from the largest term. Let us assume that the sufficient criterion for detection $\Psi^0(\mathbf{p}) > 1$ is not fulfilled. An obvious way to increase the target response is to increase the source current. This will be ineffective if one of the terms in $\delta E_x(M)$ that scale with the dipole moment dominates the uncertainty. In this case, an increase of source power will be accompanied by a corresponding increase in uncertainty if the other experimental parameters are constant. Another way to increase experimental sensitivity is to reduce the receiver noise level. The detection criterion tells us, however, that this will only be effective if the uncertainty associated with this noise dominates. When designing improved hardware, it is important to use the available resources to minimize the largest terms that contribute to uncertainty in equation 14.

What we described above was a detection criterion. The conditions for imaging by inversion will be stricter. Our imaging criterion will require another model where the target has been partially recovered. We form the data difference between the true model and this partially recovered model, and compute the ratio as in equation 17. There is some freedom in defining the model with a partially recovered target, but the transverse resistance of the resistor in this model is set to R^m percentage of the transverse resistance in the true model. Thus, the actual value of m is not known or required in our analysis. It may even be that this model cannot, in practice, be recovered by any inverse scheme. This happens if the data difference for the this model is less than the uncertainty. This leaves the

value of m undefined, but we have the answer “No” to the question we posed: Can R^m percentage of the transverse resistance of the true model be recovered by inversion for the given configuration?

The reason for formulating this in terms of transverse resistances is the well-known nonuniqueness with regards to recovering resistivity and thickness separately for a thin resistive layer. For the examples given, we have chosen $R^m = 67\%$. We could have used a stricter criterion of $R^m = 80\%$ with the effect that the maximum depth of imaging for a given parameter vector \mathbf{p} is reduced slightly from what we show here. On the other hand, if 67% of the transverse resistance of a target object is recovered, that is typically enough to distinguish it from the background. The ratio Ψ^m can serve as an imaging measure. If the remaining scattered field after m iterations is larger than the experimental uncertainty, then it is reasonable to assume that a sufficiently successful imaging has been performed.

RESULTS

Detection and imaging criteria applications

The detection and imaging criteria following from equation 17 can be used to assess the sensitivity to a given target for a specific set of experimental parameters \mathbf{p} and associated measurement uncertainty. Moreover, the uncertainty model and criteria presented can aid the design of equipment improvements to enhance the sensitivity toward specific targets. If the analysis shows that the criteria for detection or successful imaging are not fulfilled, i.e., $\Psi^m < 1$, the formalism allows us to determine the experimental component that constitutes the limiting factor. This is done by identifying the largest contribution to the uncertainty given by equation 13. We believe that such analysis can be important to make sure that equipment improvements enhance the overall sensitivity of the data. Consider the sensitivity to a faint target in a case where the dominant contribution to the uncertainty is due to calibration errors. The sensitivity will not be improved by increasing the transmitter current. This is because the uncertainty will increase with the same factor as the scattered field. From equation 17, we observe that the sensitivity is unchanged because the same factor appears in the numerator and the denominator. If, however, the dominant contribution to the uncertainty is due to a high ambient noise level, N_A , then the most effective way to increase the sensitivity will be to increase the transmitter current or dipole moment. The reason is that the

Air	
Water	0.3125 Ohm-m/0.3125 Ohm-m
Formation	1.5 Ohm-m/3.0 Ohm-m
Resistor	50 Ohm-m/50 Ohm-m or 100 Ohm-m/100 Ohm-m
Formation	2.0 Ohm-m/4.0 Ohm-m

Figure 2. The plane layer model used for the analysis of the response from a thin resistive layer embedded in a conductive background medium. Resistivity labels denote horizontal and vertical components.

nominator in equation 17 will increase, whereas the denominator is unchanged.

In addition to aiding equipment design, we believe that the detection and imaging criteria presented in this paper can be useful for CSEM feasibility studies, where one tries to assess whether the data will be able to contribute to the understanding of a certain geologic feature or hydrocarbon prospect. However, the methodology is not sufficient to determine the significance of a geologic interpretation resulting from analysis of real data. That requires a much more elaborate analysis involving inversion where a good uncertainty model is but one constituent. For example, an inaccurate interpretation could arise due to, e.g., overburden structures that are not correctly represented in the background model. The uncertainty related to the finite data resolution of overburden resistivity can then be obtained by modeling studies or stochastic inversion approaches. More generally, to assess the uncertainty of an interpretation, it is important to take into account the understanding of the geology which also incorporates analysis of other data like well logs and seismic.

We restrict the scope of this paper to consider sensitivity limitations due to equipment performance, and assume that an accurate background model is available. Below, we will apply the criteria for detection and successful imaging for specific cases. First, the methodology will be applied to determine the largest target burial depth where CSEM data provides sufficient sensitivity for detection and imaging, and identify the associated limiting experimental component. Moreover, we determine how improvements to the equipment enhance sensitivity. Dependence on target transverse resistance and water depth is also studied. We assume that the target lateral size is large enough to allow approximation by plane layer modeling. We believe that there are other interesting cases not considered below, where a similar analysis using the detection and imaging criteria can be applied. For example, it is well-known that the CSEM response is affected by finite lateral target size and shape. Sensitivity limitations due to such features could be identified by applying the detection and imaging criteria for data simulated using 3D modeling.

Reference model

We will vary target burial depth and transverse resistance to demonstrate how improvements in the instrumentation can enhance the sensitivity to a faint target. Our model is shown in Figure 2. We consider a conductive background medium, which will be a limiting factor for CSEM because signal attenuation increases with increasing conductivity. The maximum burial depths where CSEM can be used that are identified below are, as such, pessimistic estimates, because larger depths could be feasible in a more resistive formation.

In the following, we will keep the water and formation resistivities fixed. We will study CSEM data at frequency 0.25 Hz. The skin-depth in the overburden is then 1230 m. We will consider a nominal transmitter length of 270 m and a nominal transmitter elevation of 30 m. We will study source-receiver offsets up to 15 km. Although data at larger offsets could be feasible for some of the parameter sets we study, we will restrict the analysis to target depths where this range is sufficient.

Let us first consider a reference model where the transverse resistance represents a typical target for which CSEM is successfully applied with current technology. The depth from the seabed to the reservoir is chosen to be 1250 m, and the reservoir is 50 m thick. We

choose the hydrocarbon saturation to be 80%, which leads to a resistivity of 50 Ωm using the Archie model with porosity 0.3 and brine conductivity 6 S/m. The water depth is chosen to be 2000 m.

We now specify the experimental uncertainty parameters. We assume the positioning uncertainties to be $\Delta x = \pm 15$ m and $\Delta z = \pm 5$ m. The uncertainty in pitch angle is assumed to be $\Delta\theta_s = \pm 1^\circ$. This is equivalent to an elevation difference of ± 5 m comparing the head and tail electrodes. The relative uncertainties in receiver

calibration, transmitter current, and transmitter length are all assumed to be equal:

$$\left| \frac{\Delta\alpha}{\alpha} \right| = \left| \frac{\Delta J}{J} \right| = \left| \frac{\Delta L}{L} \right|. \quad (18)$$

This is roughly the case with current equipment. Also, the fact that these uncertainties influence the data quality in the same way will guide future development in the direction of making them of equal size, unless high accuracy for some of them can be achieved at a low cost. Here, we assume a constant, relative uncertainty of 1% for each of these contributions, making the total contribution equal to approximately 1.7% in the expression for $\delta E_x(c)$ in equation 13c. We will, in the following, refer to this term as the calibration uncertainty even if the term related to the transmitter length in fact is a positioning uncertainty. We will approximate that $\Delta\alpha/\alpha$ is constant for the range of electrical field strengths considered. The transmitter current is chosen to be 1 kA, and the receiver noise level is 10^{-10} V/m.

In Figure 3, we have plotted the values of uncertainty and scattered field to total uncertainty following from the expressions in equations 6, 13, 16, and 17. The curves in this and subsequent figures will have the same color coding. A legend with curve type and a tag is given in each relevant figure and is summarized in Table 1. The scattered field curve ΔE_x^0 will always be above the ΔE_x^m curve because less of the model is explained in the first iteration.

We observe in Figure 3a that, at short offsets, the total uncertainty is dominated by the contributions contained in $\delta E_x(M)$ that are proportional to the dipole moment. At large offset, the contribution ΔN_R dominates. The scattered fields are above the total uncertainty from 3 to 4 km and up to 13–14 km. The same can be seen for the plots where we normalize to the total uncertainty in Figure 3b. It is clear that we have good sensitivity in this case, and that more than 67% of the transverse resistance can be mapped by inversion. In the figure, the red line at $\Psi^m = 1$ shows the threshold level where target response falls below data uncertainty. Note that the value for Ψ^0 corresponding to the detection criterion ($\Psi^0 > 1$) is always larger than the value for Ψ^m corresponding to the stricter imaging criterion ($\Psi^m > 1$). From Figure 3a, we observe that it is the calibration related contributions $\delta E_x(c)$ that have the largest contribution to the uncertainty for offsets up to 8 km, and that the contribution from an uncertainty in the transmitter pitch $\delta E_x(\theta_s)$ has the smallest contribution.

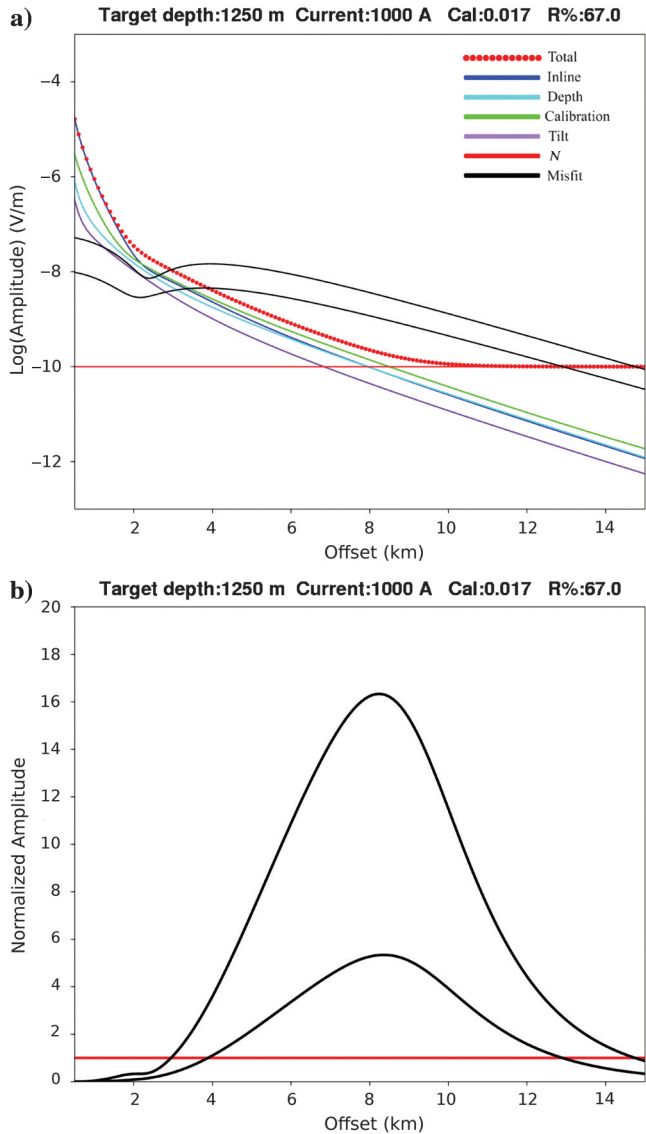


Figure 3. Data uncertainty and scattered field plots from simulated data for the reference model shown in Figure 2. The target burial depth is 1250 m. The layout of this and subsequent Figures 4–13 is (a) uncertainties and scattered field following from expressions in equations 13, 14, and 16 and color coded according to Table 1. (b) Scattered field normalized to total data uncertainty, Ψ^m from equation 17, shown in two cases for the synthetic data $n = 0$ (initial model, largest values) and $n = m$ (model with a fraction R^m of transverse resistance recovered). In (b), the solid red line corresponds to the detection and imaging criterion $\Psi^m > 1$. Note that Ψ^m corresponding to the imaging criterion is always smaller than Ψ^0 due to the reduction in the scattered field.

Table 1. Legend for the color coding in data and scattered field plots.

Contribution	Color	Tag
$\delta E_x(x)$	Blue	Inline
$\delta E_x(z)$	Cyan	Depth
$\delta E_x(c)$	Green	Calibration
$\delta E_x(\theta_s)$	Purple	Tilt/pitch
$\delta E_x(N_R)$	Red	N
$\delta E_x(\mathbf{p})$	Dotted red	Total
$\Delta E_x^0(\mathbf{p})$	Upper black	Scattered field $n = 0$
$\Delta E_x^m(\mathbf{p})$	Lower black	Scattered field $n = m$

Increased burial depth

We will now use the formalism to estimate the maximum depth of detection and the maximum depth of imaging. In the plots shown in Figure 4, we have increased the target burial depth to 2500 m. The scattered fields are now much smaller compared to the reference case in Figure 3. Note also that it is data between 6 and 12 km that contribute to Ψ^n . From Figure 4b, we conclude that 67% recovery of the transverse resistance is the limit where residual data difference is of the same magnitude as uncertainty. The maximum depth for imaging is then, by our definition, 2500 m for the given model and parameter set. This is not to be interpreted as the absolute maximum depth for imaging with the marine CSEM equipment available today because it will be model-dependent and frequency-dependent. However, this estimate is an indication of what can be achieved in a relatively conductive overburden. A rough generalization, taking frequency dependence and resistivity dependence

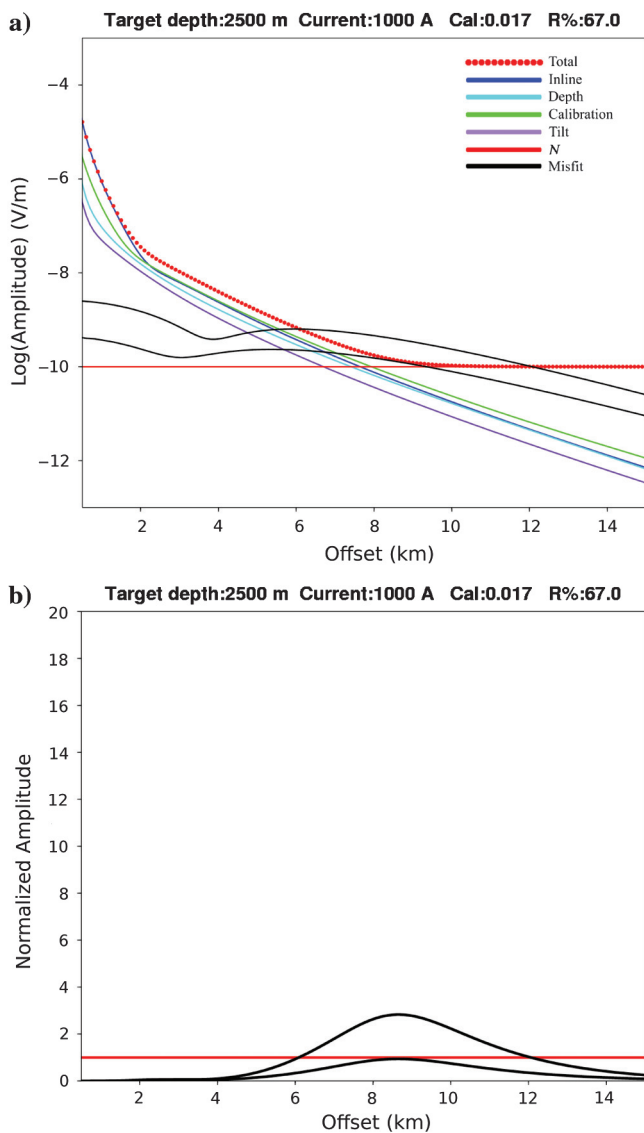


Figure 4. Target depth 2500 m. (a) Uncertainties and scattered fields. (b) Scattered field to total uncertainty, Ψ^n for $n = 0$ and $n = m$.

into consideration, is that in this case the maximum depth for imaging is twice the overburden skin-depth at 0.25 Hz. There are real data cases where we can image deeper than 2500 m at 0.25 Hz, but in those cases we usually have higher resistivities (larger skin-depths) in the overburden compared to those used for the model in Figure 2. We also note that, even if 2500 m is the maximum depth for imaging, we still have good sensitivity to detect the resistive target at this burial depth. Sensitivity is lost if the Ψ^0 curve drops below unity. For the given case, that would be at a burial depth of 3100 m.

There are several ways to increase the maximum depth for imaging. For example, the transmitter current can be increased, or the uncertainty level of the experimental parameters can be reduced. Specifically, this could be to reduce the receiver noise level, the positioning uncertainty, or the calibration uncertainty. In practice, all of these improvements will require changes to the experimental equipment in use today.

Let us start by analyzing the effect of reducing the receiver self-noise. The receiver noise level ΔN_R is reduced with a factor of 10 in Figure 5 compared to Figure 4. The burial depth is also increased to 3000 m. The curves indicate that imaging of a thin resistor at this burial depth is possible. It is the data at offsets above 7.5 km that are driving the inversion.

Our next scenario is that the transmitter current is increased from $J = 1$ to 10 kA. The result is shown in Figure 6. The other difference compared to Figure 5 is that the burial depth of the thin resistor is increased from 3000 to 3500 m. The data for large source-receiver offsets have a significant response. The data are above the uncertainty limit even at these large offsets, so this is a situation where imaging is possible, but note that 3D effects due to a finite target size may alter this situation. In the scenario we study here, we assume that the target response can be approximated from a plane layer model up to a very large burial depth. It is reasonable to assume that at least resistors with a large surface area can be imaged for the configuration used for Figure 6.

Comparison of the results in Figures 5 and 6 shows that there is a different effect from reducing the receiver noise level and increasing the transmitter current. Reducing the receiver noise level has few side effects and the total uncertainty is reduced at all source-receiver offsets, but with larger effect at large offsets where the contribution $\delta E_x(N_R)$ dominates. Increasing the transmitter current will also increase the total uncertainty, in particular at small and intermediate offsets. This is due to the contributions of $\delta E_x(M)$ in equation 15 that scale with transmitter dipole moment. Hence, we cannot make full use of the increased signal strength unless we can simultaneously reduce the navigation and calibration uncertainties.

A reduction in the receiver noise level with a factor of 10 and an increase in the source output with a factor of 10 is technically feasible. In fact, we have a surface-towed transmitter with an output of 7.2 kA in operation today. A deep-towed transmitter with an output of 10 kA is a challenge for the future. If these are the only two improvements introduced, then the maximum depth of imaging will be slightly above 3500 m at 0.25 Hz. The limiting factors with such a configuration are those contributions to the uncertainty that scale with the electric field or the derivative of the electric field. The calibration uncertainty $\delta E_x(c)$ must be reduced to fully exploit the potential increase in transmitter current with a factor of 10. From Figure 6, we observe that the largest contribution to the uncertainty is the calibration term (green curve). We observe in Figure 6 that

$\delta E_x(c)$ is larger than the additive noise term ΔN_R (solid red curve) for all offset up to 14.6 km. If we assume that our goal is to design equipment that can image to larger depths than 3500 m, then we conclude from Figure 6 that a further reduction in ΔN_R will not suffice because the dominating term $\delta E_x(c)$ is unaffected by this reduction. A further increase in the transmitter current will increase the magnitude of the target response, but also the magnitude of all uncertainty terms that are proportional to the emitted field strength. The result is that the curves in Figure 6b are preserved because the numerator and the denominator of equation 17 are multiplied with the same factor. We need to make the denominator smaller to increase the value of Ψ^n . Increased imaging depth cannot be achieved unless the dominating term $\delta E_x(c)$ is reduced as a first step.

From equation 13c, we see that for the first step in equipment refinement we must focus our attention on the receiver calibration, the transmitter current measurement, and the transmitter length

measurement. We will need to address all three issues if the present state of the equipment is as described in equation 18. It may be the receiver unit that needs improvement, but alternatively it may be that the calibration procedures for the receiver need improvements. In the latter case, no change to the receiver itself is required, but the hardware for onboard, predrop, calibration of the receiver must be improved. In short, we may need an improved voltmeter for on-board receiver calibration. The transmitted current must be known with better accuracy. Again, this does not necessarily imply any modification of the main transmitter hardware, but an improvement in the accuracy of the measurement of the transmitted current. The issue can be that we need a more accurate ampere meter for the transmitter current measurement.

Finally, the uncertainty in the transmitter length measurement must be reduced. One solution may be to increase the number of

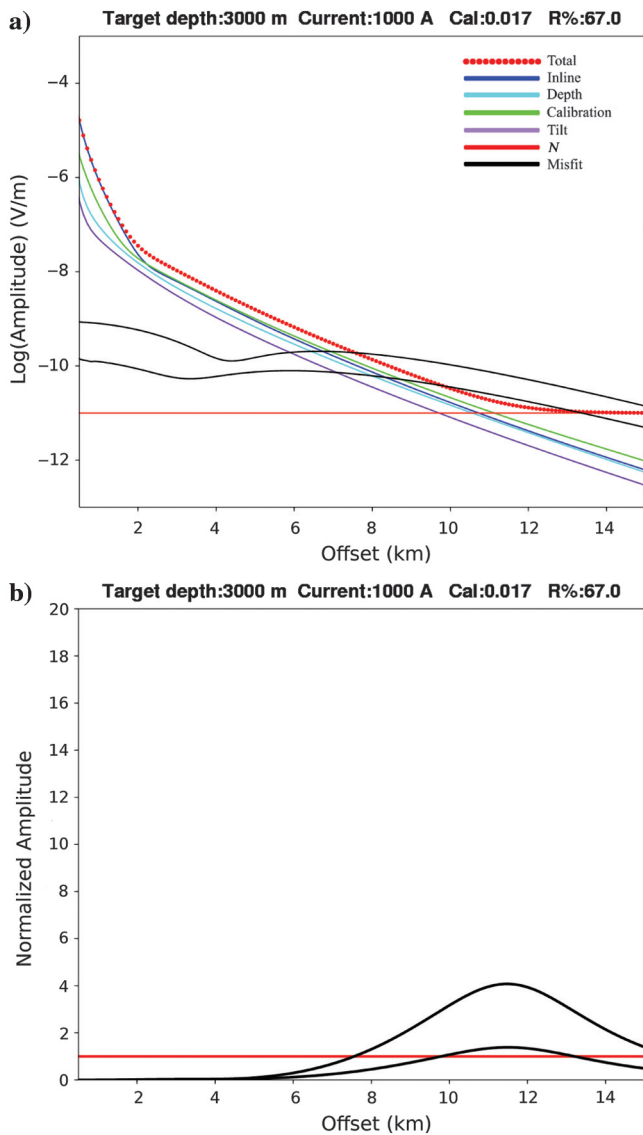


Figure 5. Target depth 3000 m, decreased noise level $\Delta N_R = 10^{-11}$ V/m. (a) Uncertainties and scattered fields. (b) Scattered field to total uncertainty, Ψ^n for $n = 0$ and $n = m$.

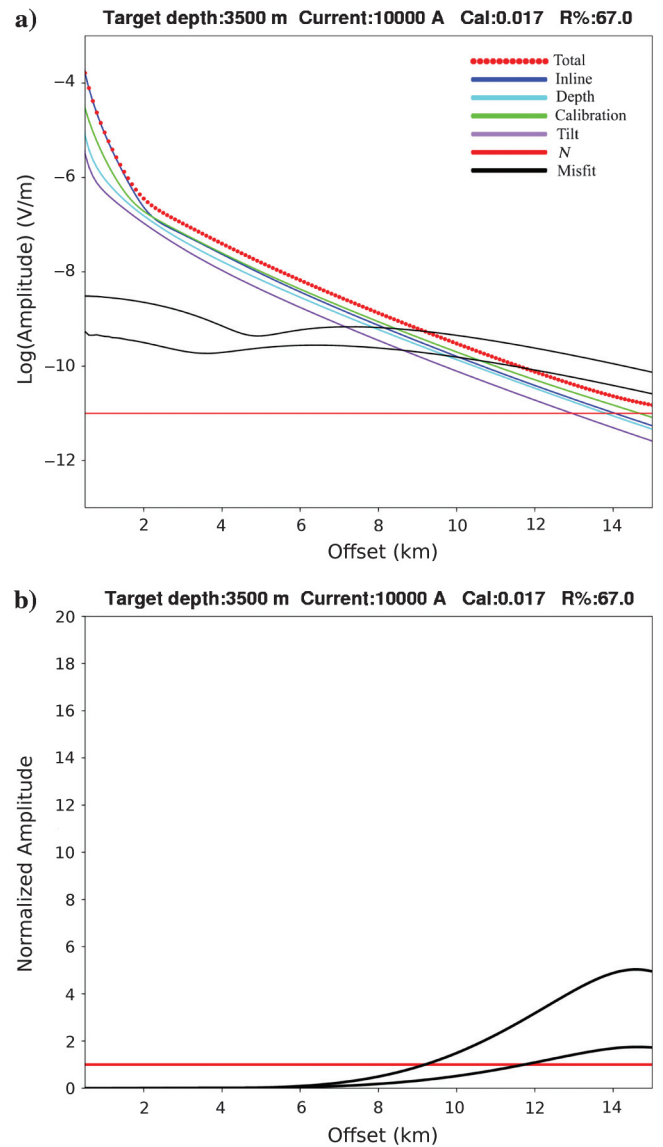


Figure 6. Target depth 3500 m, decreased noise level $\Delta N_R = 10^{-11}$ V/m and increased current $J = 10$ kA. (a) Uncertainties and scattered fields. (b) Scattered field to total uncertainty, Ψ^n for $n = 0$ and $n = m$.

acoustic devices used in this measurement together with an upgrade of hardware and software methods. Each of these issues must be analyzed properly. Figure 6, in combination with equation 13c, tell us that we are not going anywhere unless we make improvements that reduce the added effect of these three uncertainty contributions. In Figure 7, we show the effect of reducing each of these three uncertainties from 1% to 0.3%. The reduction in the total uncertainty is not sufficient to increase the maximum depth of imaging significantly. The total uncertainty is now dominated by the term related to uncertainty in the inline position (blue curve). Uncertainty in inline position is given by equation 13a. We also note that the curve for transmitter depth uncertainty (cyan curve) is of a magnitude similar to the inline position uncertainty curve. Uncertainty in transmitter depth is given by equation 13b. The second step in equipment

refinement is obviously to improve transmitter navigation, in terms of measuring transmitter inline position and in terms of measuring transmitter depth. We cannot give details on the technical solutions here, but note that Figure 7 tells where to have the focus in the second stage of equipment development.

Figure 8 shows the effect of reducing the uncertainty in the inline position Δx from ± 15 to ± 5 m, and the uncertainty related to transmitter depth Δz from ± 5 to ± 2 m. The dominating term is now the contribution related to transmitter pitch (pink curve). This contribution was the smallest term if we look back at Figure 6, which is also for a target burial depth of 3500 m. It is this pitch uncertainty problem that must be solved next. For the purpose of reducing the total uncertainty significantly, it is of little use to work further on improving the other parts of the system if minimizing the

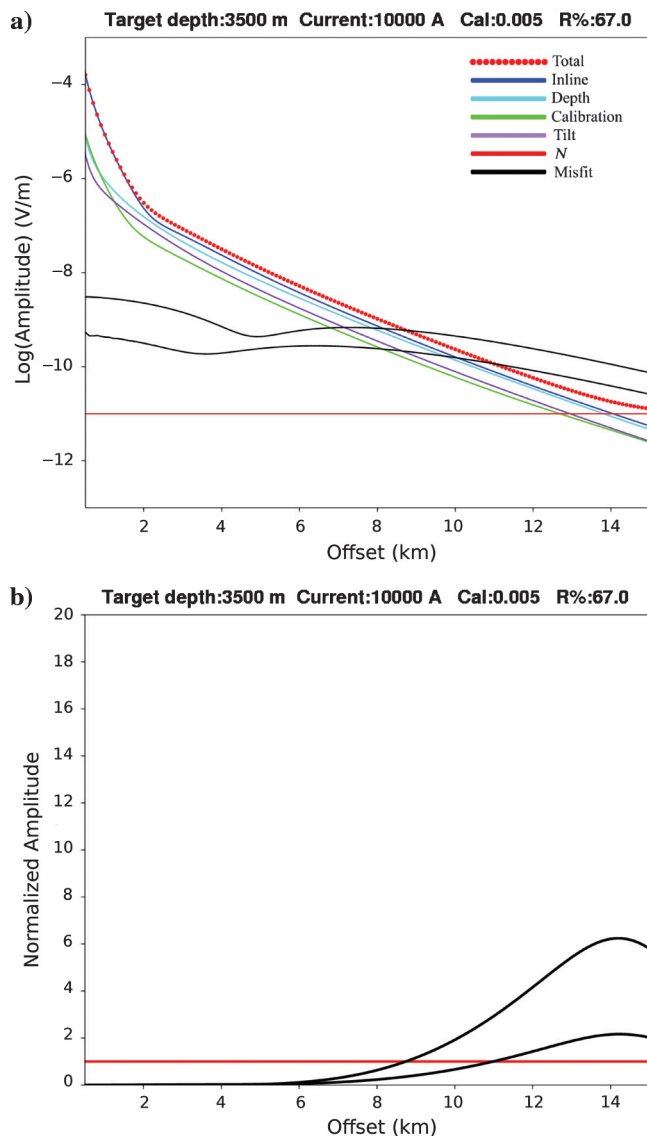


Figure 7. Target depth 3500 m, decreased noise level $\Delta N_R = 10^{-11}$ V/m, increased current $J = 10$ kA, and decreased calibration errors $|\Delta\alpha/\alpha| = 0.3$. (a) Uncertainties and scattered fields. (b) Scattered field to total uncertainty, Ψ^n for $n = 0$ and $n = m$.

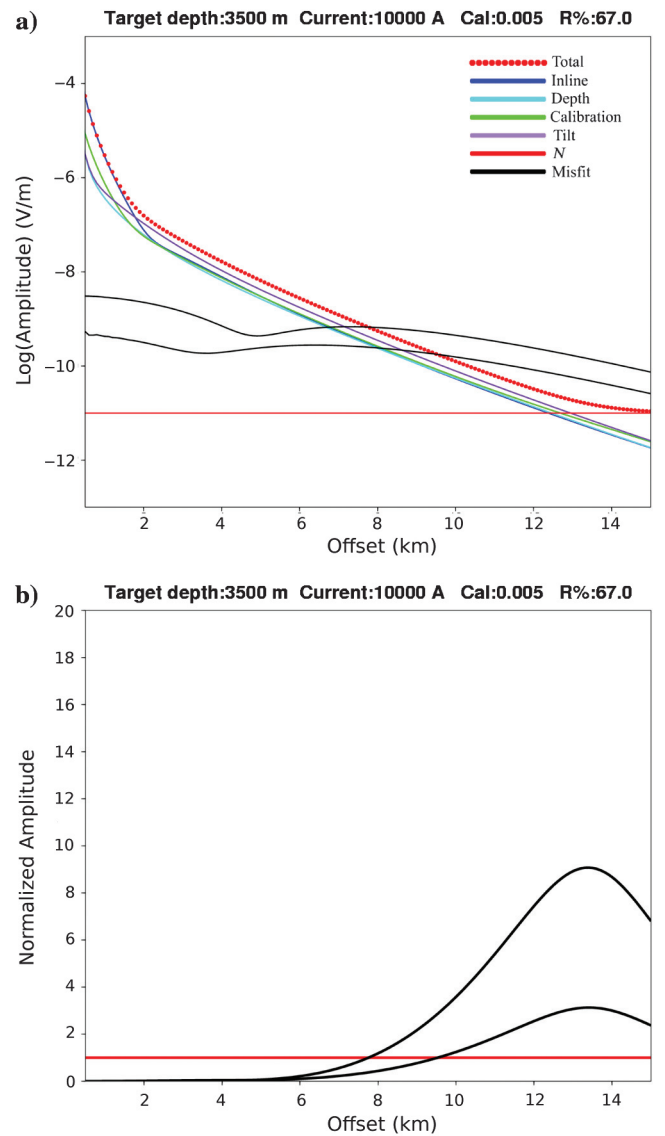


Figure 8. Target depth 3500 m, decreased noise level $\Delta N_R = 10^{-11}$ V/m, increased current $J = 10$ kA, decreased calibration errors $|\Delta\alpha/\alpha| = 0.3$, and decreased positioning errors $\Delta x = \pm 5$ m and $\Delta z = 2$ m. (a) Uncertainties and scattered fields. (b) Scattered field to total uncertainty, Ψ^n for $n = 0$ and $n = m$.

total uncertainty is the goal. This may again be a navigation-related issue where improved accuracy in pitch measurement is required. This uncertainty can also be solved by how the transmitter is designed. A trivial example is a surface-towed transmitter where the uncertainty in pitch is very small because potential vertical movement of the transmitter antenna is restricted by the design of the system. The inversion data difference normalized to uncertainty plotted in Figure 8b shows that the main part of the transverse resistance for a resistor 3500 m below the seabed can be imaged with good margins.

The resistivity model used for Figure 9 differs from the model used in Figure 8 by the fact that the resistor is buried at 4000 m below the seabed. The uncertainty in pitch angle has been assumed to be ± 1 degree, up to and including the examples in Figure 8. As mentioned, this is equivalent to an elevation difference of ± 5 m comparing the head and tail electrodes. For the examples in Figure 9, we have assumed that this uncertainty is reduced to ± 2 m, which equals an uncertainty of ± 0.4 degrees. Figure 9b indicates that imaging of laterally large resistors at the burial depth of 4000 m in a fairly conductive background formation is possible. This gives a maximum depth of imaging that is 3.25 times the overburden skin-depth at 0.25 Hz. The maximum depth of detection is 5000 m for this case. This is when Ψ^0 drops below 1 for all offsets.

Increased transverse resistance

The transverse resistance for the target has been $2500 \Omega\text{m}^2$ up to this point. This is a conservative value. The resistor in Constable's canonical oil-field model (Constable, 2010) has a transverse resistance of $10,000 \Omega\text{m}^2$. This is not an unrealistic value, but represents, e.g., a 100-m-thick hydrocarbon reservoir with high saturation and resistivity $100 \Omega\text{m}$. Keeping all other parameters equal to those used for Figure 9, this target is well within the imaging threshold with $\Psi^m(\mathbf{p}) > 1$ for several kilometers offset. The necessary improvements on current equipment are technically feasible. The largest cost is for increasing the transmitter output current from 1 to 1.5 kA, which is typical today to 10 kA.

Figure 10 shows the effect of having the $10,000 \Omega\text{m}^2$ resistor at a burial depth of 5 km below the seabed. The plots show that imaging at this large depth is possible given that the equipment is good enough. In a real case, we would normally expect the background resistivity to increase with depth, in particular when the depth range is as large as 5 km. This certainly helps with the sensitivity at large depths, and the effect makes it probable that imaging a large hydrocarbon reservoir at a depth of 5 km can succeed given the next generation of marine CSEM equipment.

Shallow water

The maximum depth of imaging is reduced when the water depth is reduced. Our shallow-water case will have water depth reduced from 2000 to 40 m, and the noise level is increased by a factor of 100 compared to the deep-water case. This noise level is no longer representative for the receiver self-noise, but includes the effect of residual MT noise that is not removed, and potential swell noise and vibration noise. If we consider the same model and experimental uncertainty parameters as in Figure 10 where the burial depth is 5000 m, the scattered field will be smaller than the noise level on all offsets. It is obvious that there is no sensitivity to the target resistor in this case.

In shallow water, the airwave effect leads to higher amplitudes for the electric field at intermediate and large offsets. The impact of uncertainty contributions that scale with the field amplitude is therefore huge. However, some of these contributions can be assumed much smaller in the shallow water case because the acquisition may be simpler. For example, the transmitter can be surface-towed so that each electrode can be positioned with GPS. The surface towing minimizes the uncertainty in transmitter pitch, and the GPS system can be used to minimize the uncertainty in transmitter length (Shantsev et al., 2010). This is equipment that is in place and used for marine CSEM surveying today. The receivers are also much easier to position accurately in shallow water. In Figure 11, we have assumed that all navigation uncertainties are below ± 1 m

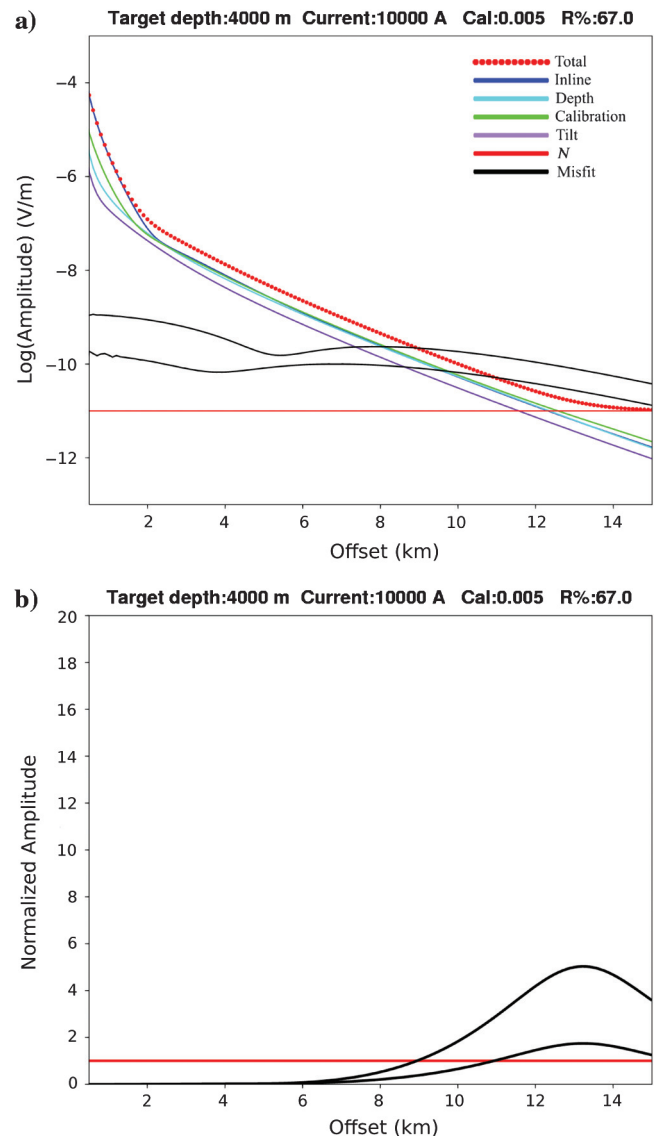


Figure 9. Target depth 4000 m, decreased noise level $\Delta N_R = 10^{-11}$ V/m, increased current $J = 10$ kA, decreased calibration errors $|\Delta\alpha/\alpha| = 0.3$, decreased positioning errors $\Delta x = \pm 5$ m and $\Delta z = 2$ m, and reduced pitch error $\Delta\theta_s = \pm 0.4^\circ$. (a) Uncertainties and scattered fields. (b) Scattered field to total uncertainty, Ψ^m for $n = 0$ and $n = m$.

for a surface-towed source in 40 m of water depth. The target resistor is moved to a depth of 3700 m. The scattered fields are well above the noise level to large offsets, and it is the calibration uncertainties that determine the amplitude of the total uncertainty. From Figure 11b, we conclude that the resistor can be properly imaged in this case.

We can connect back to Figure 4 and the parameters used to generate those curves. Figure 12 shows the same case, but with 40 m of water depth. The resistor has a transverse resistance of $2500 \Omega\text{m}^2$, as is the case in Figure 4, but is at a depth of 2200 m. The additive noise level is a factor of 10 larger in Figure 12, compared to Figure 4. Note the increase in the scattered field for the shallow water case. The scattered field is an order of magnitude larger in the shallow-water case. Most of this effect is due to the increased response to a thin resistor in shallow water as discussed in Mittet

(2008), and not due to the fact that the resistor depth has changed from 2500 to 2200 m. Figure 12b indicates that a thin resistor can be properly imaged at a burial depth of 2200 m below the seabed in a water depth of 40 m and in a conductive formation. In fact, a surface-towed system can be used. The increased positioning accuracy leads to an increased maximum depth of imaging. This is shown in Figure 13. The difference from Figure 12 is that all navigation uncertainties are below ± 1 m. The maximum depth of imaging is then 2400 m, which is only 100 m less than for the deep-water case.

There is a difference when we compare the change of maximum depth of imaging in deep and shallow water for current equipment specifications and the proposed next generation systems. For current equipment, the maximum depth of imaging is reduced by 100 m in shallow water, and for next generation systems with characteristics as used for Figures 10 and 11 by 1300 m. The main effect

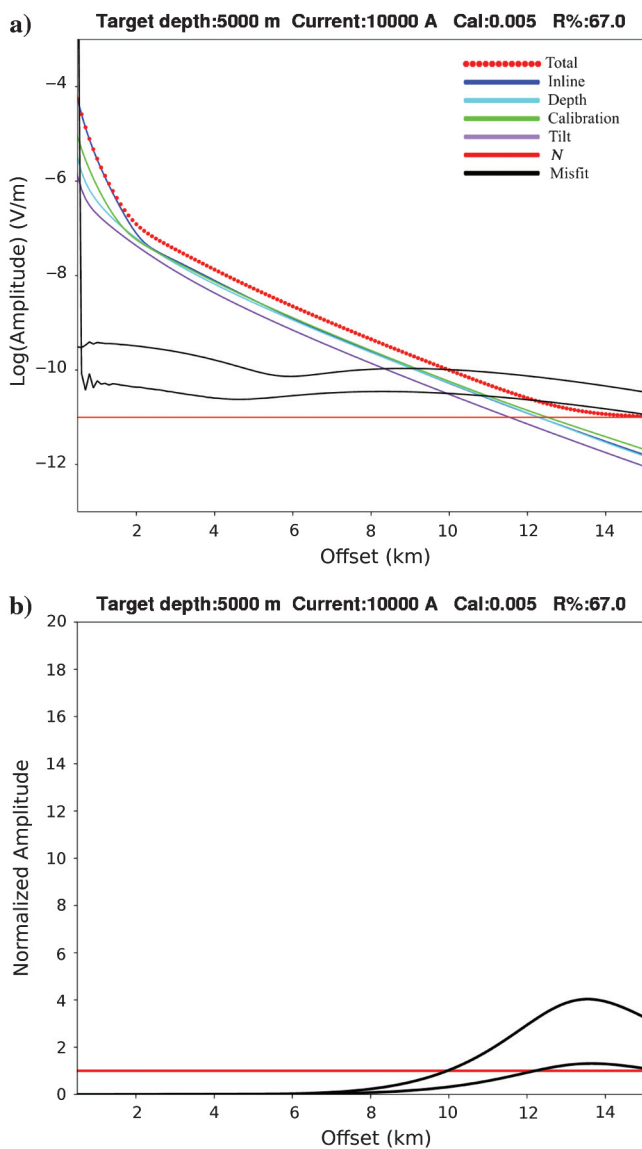


Figure 10. Target depth 5000 m, increased transverse resistance $10,000 \Omega\text{m}^2$. (a) Uncertainties and scattered fields. (b) Scattered field to total uncertainty, Ψ^n for $n = 0$ and $n = m$.

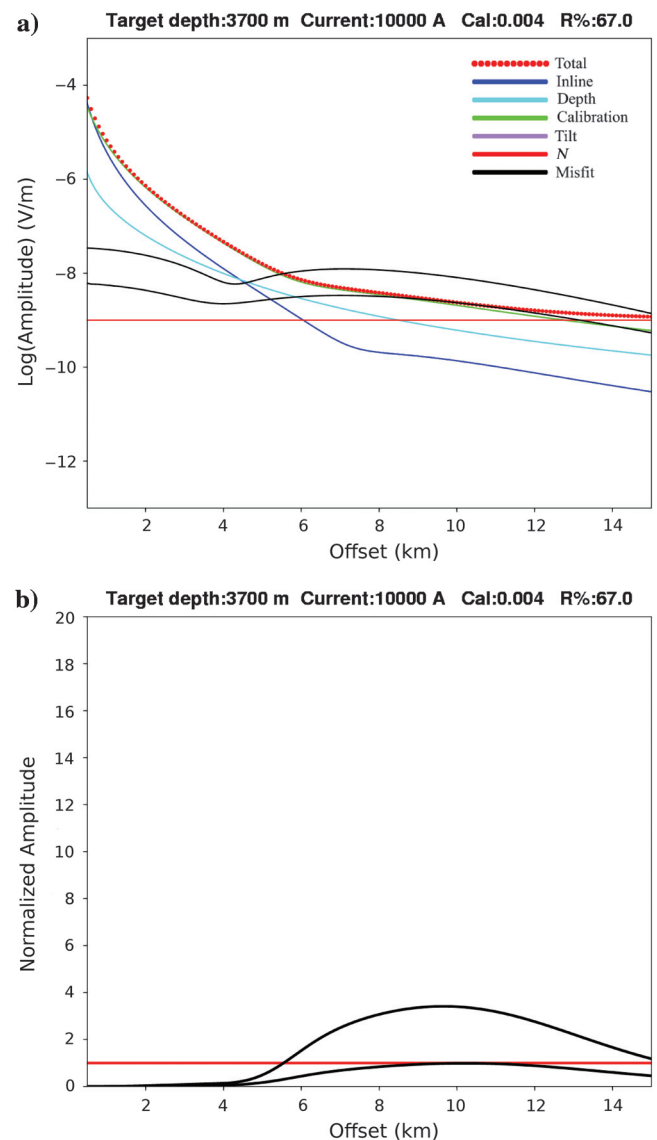


Figure 11. Target depth 3700 m, shallow-water case. Navigation uncertainties reduced to ± 1 m, otherwise same uncertainty parameters as in Figure 10. (a) Uncertainties and scattered fields. (b) Scattered field to total uncertainty, Ψ^n for $n = 0$ and $n = m$.

is caused by the low noise level ΔN_R that is assumed for the case in Figure 10. This makes it possible to image thin resistors at large depth. In shallow water, the noise level is dominated by effects other than the receiver self-noise, and the noise levels used for the shallow-water cases in Figure 11 and Figure 13 are identical. The maximum depth of imaging is 4100 m instead of 5000 m if the receiver self noise is assumed to be 10^{-10} V/m instead of 10^{-11} V/m for the deep-water case in Figure 10. That makes a difference of only 400 m in maximum depth of imaging between the deep-water and the shallow-water cases. Thus, the benefits of reducing the receiver self-noise is largest in deep water. In shallow water, we have to assume that the noise level is larger due to sources other than the receiver, and an increased maximum depth of imaging can be achieved by an increase in the source current combined with improved positioning accuracy and improved calibration accuracy.

Approximate larger offset uncertainty model

The sum of uncertainty contributions proportional to the field or its partial derivatives has a fairly simple behavior for intermediate and large offsets when we assume that the relative uncertainties in equation 18 are constants. This can be seen by taking the ratio of $\delta E_x(M)$ from equation 18 to the total inline field in equation 1. This ratio γ , as a function of source-receiver offset x , is

$$\gamma(x) = \frac{\delta E_x(x|M)}{|E_x(x)|} \tag{19}$$

This ratio is shown in Figure 14. In Figure 14a, it is plotted for the parameters used to generate the curves in Figure 4 and represent the status of equipment used today. As can be seen, for offsets above

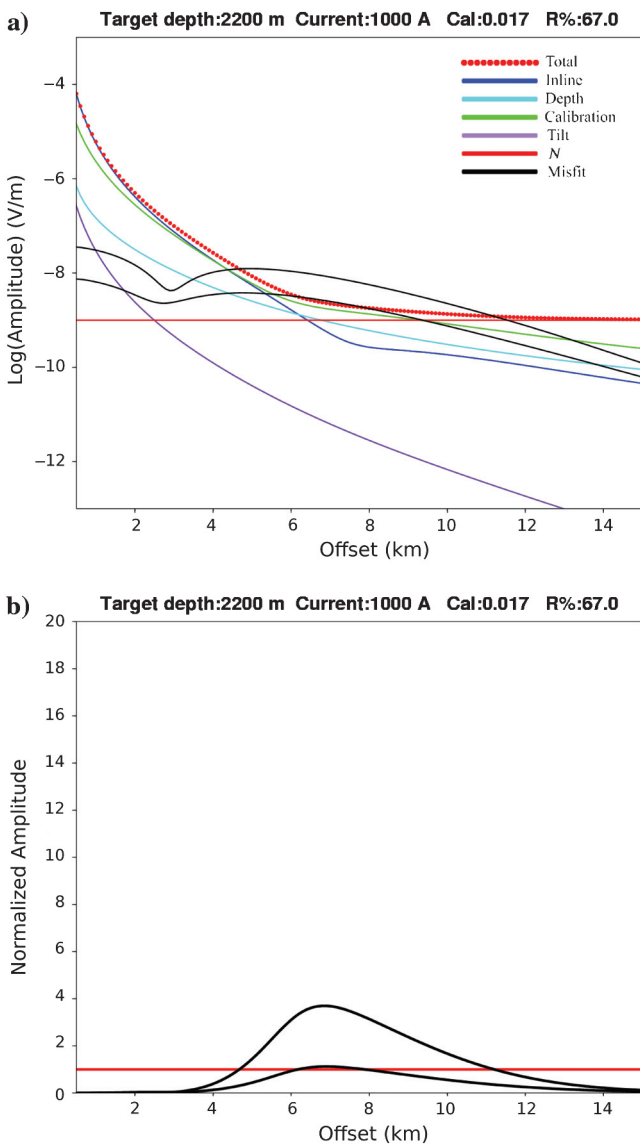


Figure 12. Target depth 2200 m, shallow-water case. Experimental uncertainty levels similar to Figure 4, representing current equipment. (a) Uncertainties and scattered fields. (b) Scattered field to total uncertainty, Ψ^n for $n = 0$ and $n = m$.

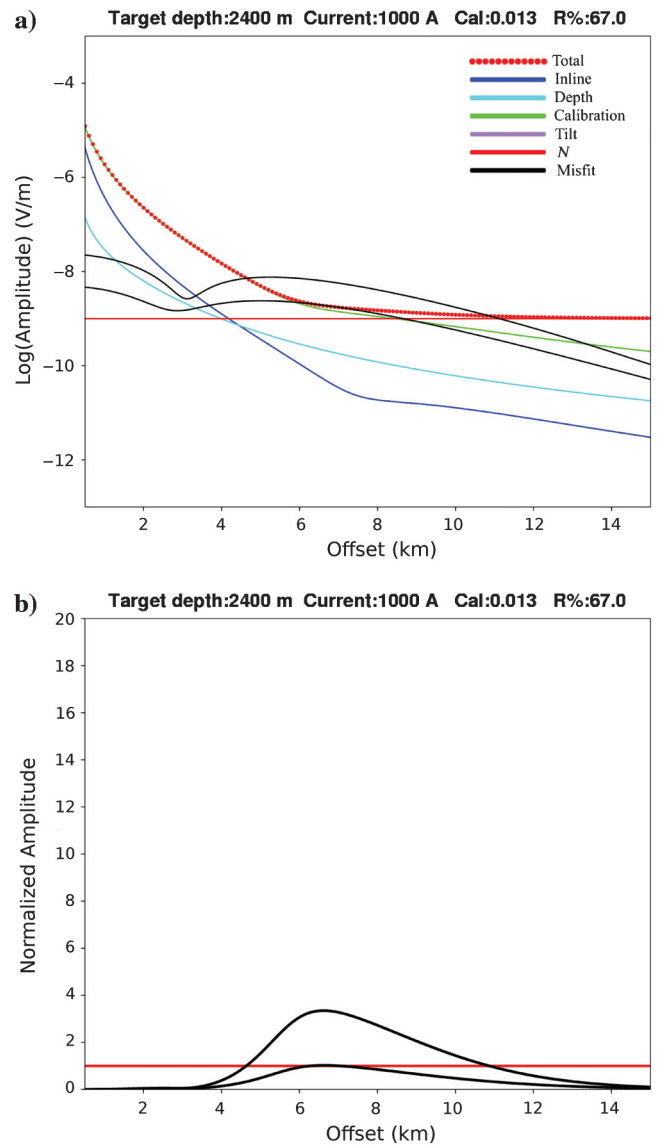


Figure 13. Target depth 2400 m, shallow-water case. Experimental uncertainty levels reflect current surface towed systems. (a) Uncertainties and scattered fields. (b) Scattered field to total uncertainty, Ψ^n for $n = 0$ and $n = m$.

Downloaded 12/07/12 to 62.92.124.145. Redistribution subject to SEG license or copyright; see Terms of Use at http://library.seg.org/

2 km the ratio is close to constant and at a value of 0.03. The curve in Figure 14b is plotted for the parameters used to generate the curves in Figure 9 and represent the properties of an equipment set required to image down to 4–5 km. The ratio is close to 0.01 for offsets above 2 km.

It is reasonable to approximate the total uncertainty in the offset range that contributes to inversion as

$$\delta E_x(x) = \sqrt{\gamma^2 |E_x(x)|^2 + \Delta N^2}. \quad (20)$$

This is based on the behavior found in Figure 14 and where now γ and ΔN_R are two fixed values. This makes a recipe for increasing the depth of imaging of approximately 2.5 km, which we have today, to 4–5 km: Reduce receiver noise level by a factor of 10; increase the source current with a factor 10; and reduce the combined

contribution to the relative uncertainty due to calibration, current, and transmitter positioning from 3% to 1%.

Another approximation that is sometimes used to determine the total uncertainty is

$$\delta E_x(x) = \gamma |E_x(x)| + \Delta N_R. \quad (21)$$

This approximation gives an estimate similar to the expression in equation 20 when one of the terms on the right-hand side dominates, and a larger estimate otherwise. We believe the estimate from equation 20 to be more accurate because this expression is consistent with the addition of variances in probability theory, whereas the expression in equation 21 is not. In practice, the estimates in equations 20 and 21 will differ significantly only over a short offset interval. This is because the term proportional to the field amplitude is damped exponentially and rapidly changes magnitude.

CONCLUSIONS

We have developed a formalism to study how experimental uncertainty affects CSEM data. We use this formalism to formulate criteria for detection and imaging of resistive targets. These criteria determine maximum burial depths to detect and image hydrocarbon reservoirs given a set of parameters that describe the model and the experimental equipment. For equipment sets currently in use, we estimate that for a 50-m-thick reservoir with hydrocarbon saturation 80% embedded in a conductive formation, the maximum burial depth with successful imaging is 2500 m in deep water and 2400 m in shallow water. These depths are approximately at twice the skin depth for the overburden and frequency we have considered here. Furthermore, we describe how our formalism can be used to analyze other cases where sensitivity is an issue due to, e.g., 3D effects.

We then study how the next generation CSEM hardware can be improved most efficiently to increase sensitivity and maximum depth for detection and imaging. Considering a large 100-m-thick reservoir with hydrocarbon saturation 80%, we suggest specifications that are feasible today, and which will increase the maximum burial depth with successful imaging to 5000 m in deep water and 3700 m in shallow water. This can be obtained by reducing the receiver noise level by a factor of 10, increasing the source current amplitude by a factor of 10, and reducing the relative uncertainty from contributions that scale by dipole moment by a factor of three.

Our analysis can be used to identify experimental limiting factors and to guide development of next generation CSEM equipment. Moreover, we believe that the suggested formalism can be useful for feasibility studies, and to formulate experimental requirements for CSEM time-lapse.

ACKNOWLEDGMENTS

We thank Hans Roger Jensen, Peter van der Sman, Mark Rosenquist, and Mathieu Darnet for helpful discussions. We also thank EMGS ASA for permission to publish this work. The comments from three anonymous reviewers helped us to improve the quality of the paper.

REFERENCES

- Constable, S., 2010, Ten years of marine CSEM for hydrocarbon exploration: *Geophysics*, **75**, no. 5, A67–A81, doi: [10.1190/1.3483451](https://doi.org/10.1190/1.3483451).
de la Kethulle de Ryhove, S., and F. Maaø, 2008, On the removal of MT signals from SBL data: 70th Annual Conference and Exhibition, EAGE, Extended Abstracts, H047.

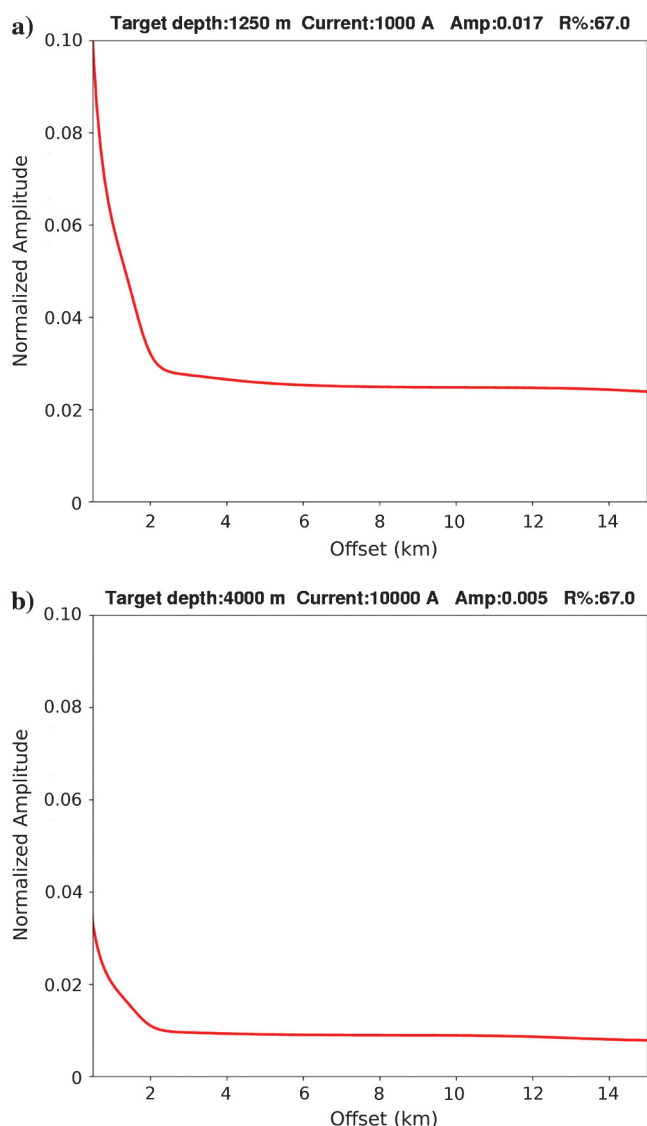


Figure 14. Ratio between uncertainty terms scaling with dipole moment, $E_x(M)$, and total field amplitude $|E_x|$. The parameters used to generate these curves reflect (a) current equipment, and (b) equipment required to image targets at 4–5-km burial depth.

- Eidesmo, T., S. Ellingsrud, L. M. MacGregor, S. Constable, M. C. Sinha, S. Johansen, F. N. Kong, and H. Westerdahl, 2002, Sea bed logging (SBL), a new method for remote and direct identification of hydrocarbon filled layers in deepwater areas: *First Break*, **20**, 144–152.
- Ellingsrud, S., T. Eidesmo, M. C. Sinha, L. M. MacGregor, and S. Constable, 2002, Remote sensing of hydrocarbon layers by seabed logging (SBL): Results from a cruise offshore Angola: *The Leading Edge*, **21**, 972–982, doi: [10.1190/1.1518433](https://doi.org/10.1190/1.1518433).
- Mittet, R., 2008, Normalized amplitude ratios for frequency-domain CSEM in very shallow water: *First Break*, **26**, 47–54.
- Morten, J. P., and A. K. Bjørke, 2010, Fast-track marine CSEM processing and 3D inversion: 72nd EAGE Conference and Exhibition, Extended Abstracts, C004.
- Morten, J. P., A. K. Bjørke, and T. Støren, 2009, CSEM data uncertainty analysis for 3D inversion: 79th Annual International Meeting, SEG, Expanded Abstracts, 724–728.
- Myer, D., S. Constable, and K. Key, 2010, Marine CSEM of the Scarborough Gas Field: 80th Annual International Meeting, SEG, Expanded Abstracts, 665–669.
- Orange, A., K. Key, and S. Constable, 2009, The feasibility of reservoir monitoring using time-lapse marine CSEM: *Geophysics*, **74**, no. 2, 21–29, doi: [10.1190/1.3059600](https://doi.org/10.1190/1.3059600).
- Shantsev, D. V., F. Roth, C. Twarz, A. Frisvoll, and A. K. Nguyen, 2010, Shallow water CSEM using a surface-towed source: 72nd EAGE Conference and Exhibition, Extended Abstracts, C018.
- Zach, J. J., M. A. Frenkel, D. Ridyard, J. Hincapie, B. Dubois, and J. P. Morten, 2009, Marine CSEM time-lapse repeatability for hydrocarbon field monitoring: 79th Annual International Meeting, SEG, Expanded Abstracts, 820–824.